

See discussions, stats, and author profiles for this publication at: <https://www.researchgate.net/publication/272509530>

# Ion Transport in Na<sub>2</sub>M<sub>2</sub>TeO<sub>6</sub>: Insights from Molecular Dynamics Simulation

ARTICLE in THE JOURNAL OF PHYSICAL CHEMISTRY C · JANUARY 2015

Impact Factor: 4.77 · DOI: 10.1021/jp5094349

CITATION

1

READS

85

## 2 AUTHORS:



Kartik Sau

Indian Institute of Technology Guwahati

3 PUBLICATIONS 1 CITATION

SEE PROFILE



Padmanabhan Padma Kumar

Indian Institute of Technology Guwahati

33 PUBLICATIONS 639 CITATIONS

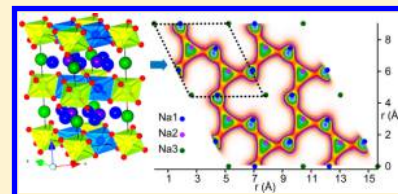
SEE PROFILE

# Ion Transport in $\text{Na}_2\text{M}_2\text{TeO}_6$ : Insights from Molecular Dynamics Simulation

Kartik Sau and P. Padma Kumar\*

Department of Physics, Indian Institute of Technology, Guwahati, India

**ABSTRACT:** An interatomic potential is proposed for the recently discovered family of superionic solids of the formula  $\text{Na}_2\text{M}_2\text{TeO}_6$ , where  $\text{M} = \text{Ni}, \text{Zn}, \text{Co},$  or  $\text{Mg}$ . Molecular dynamics simulations demonstrating the quality of the potential in reproducing various structural and transport properties of this promising class of materials is presented. The study provides fresh insights on the microscopic energetics and  $\text{Na}^+$  migration pathways. Strong ion–ion correlations, resulting in a highly cooperative conduction mechanism, emerge from the study.



## INTRODUCTION

Development of high-energy-density batteries, fuel cells,<sup>1,2</sup> and super capacitors are an integral part of renewable energy technologies<sup>3</sup> to replace the conventional fossil fuels. Fast ion conductors (FICs) form a critical component of these devices and are a lead topic of concurrent academic and industrial research.<sup>4–7</sup> Extensive studies in the last three decades have resulted in significant advances in the development of high-energy-density batteries, largely of  $\text{Li}^+$  conducting materials.<sup>8–17</sup> Lithium is, however, expensive, and its reserves are of rather limited accessibility.<sup>18</sup> Alternatively, sodium conducting materials are more promising for energy storage applications as it is naturally abundant and has a suitable redox potential.<sup>19</sup> Thus, development of sodium conducting FICs working at ambient temperatures is gaining renewed attention.<sup>17</sup>

One of the major challenges<sup>20,21</sup> in the search for improved FICs is the lack of microscopic information related to the conduction mechanism,<sup>22</sup> which limits our understanding of factors that control the ion transport. The search for better FICs is, thus, largely guided by intuition. Alternatively, computational techniques such as molecular dynamics (MD) simulations, can complement the experimental efforts in this pursuit, providing a great deal of valuable microscopic information related to ion transport.<sup>23</sup> Molecular dynamics studies on silver iodide<sup>24,25</sup> and on  $\beta$ -alumina<sup>26</sup> are two classic examples from early literature. The technique has been successfully used in the past in the study of a variety of oxide ion conductors as well.<sup>27,28</sup>

More recently, employing molecular dynamics simulations we have predicted that the ordering of framework ions (“immobile” ions) in aliovalently substituted materials can have a profound influence on the ionic conductivity. MD simulations on  $\text{Na}_3\text{Zr}_2\text{Si}_2\text{PO}_{12}$  (NASICON) having different Si/P ordering in the unit cells differed in their conductivities by more than an order of magnitude.<sup>29</sup> Simulations on  $\text{Na}_2\text{Zr}_2\text{SiP}_2\text{O}_{12}$  suggested that Si/P ordering can also influence the nature of ion transport, such as from a near isotropic to a predominantly two-dimensional ionic conduction.<sup>30</sup> Similar behavior was evidenced in oxide ion conductors,  $\text{Gd}_{0.5}\text{Ba}_{0.5}\text{MnO}_{3-\delta}$  and  $\text{GdBaCo}_2\text{O}_{5+\delta}$ , respectively, in the

experimental studies of Taskin et al.,<sup>31,32</sup> and MD simulations of Parfitt et al.<sup>33</sup> These studies suggest that suitable heat treatment of the sample, among other possible strategies, could result in favorable ordering of framework ions to enhance ion transport in the matrix.

While molecular dynamics have been very useful in understanding microscopics of ion transport, the lack of a generic recipe for the development of interatomic potential and the poor transferability of the interaction parameters between species across different systems remain major hurdles in carrying out the simulations.

The present modeling and MD simulations is motivated by the recent experimental studies of Evstigneeva et al.<sup>34</sup> who synthesized a family of  $\text{Na}^+$  conducting fast ion solids<sup>35,36</sup> of the formula,  $\text{Na}_2\text{M}_2\text{TeO}_6$ , where  $\text{M} = \text{Ni}, \text{Zn}, \text{Co}$  or  $\text{Mg}$ .  $\text{Na}_2\text{M}_2\text{TeO}_6$  consists of edge shared  $\text{M}-\text{O}$  and  $\text{Te}-\text{O}$  octahedral layers spanning the  $ab$ -plane, with the  $\text{Na}^+$  ions occupying the interlayer. The Ni-containing composition shows highest ionic conductivity of the family ( $\sigma = 0.11\text{S/cm}$  at 573 K, which compares well with the  $\beta$ -alumina<sup>37–40</sup>) and promises scope for further improvements through ion substitutions.<sup>41</sup> The present study provides an accurate interatomic potential for the family of  $\text{Na}_2\text{M}_2\text{TeO}_6$ , where  $\text{M} = \text{Ni}, \text{Co}, \text{Zn},$  or  $\text{Mg}$ , and fresh insights on ion transport in them is derived, focusing on the highest conducting  $\text{Na}_2\text{Ni}_2\text{TeO}_6$ .

## METHODOLOGY

**Interatomic Potential.** We employ the Vashishta-Rahman form of the interatomic potential that have performed remarkably well for a variety of systems, such as,  $\text{AgI}$ ,<sup>42–45</sup>  $\text{Ag}_2\text{Se}$ ,<sup>24,25</sup> and NASICONs,<sup>29,46,47</sup> and is given by

$$V_{ij}(r_{ij}) = \frac{q_i q_j}{r_{ij}} + \frac{A_{ij}(\sigma_i + \sigma_j)^{n_{ij}}}{r_{ij}^{n_{ij}}} - \frac{P_{ij}}{r_{ij}^4} - \frac{C_{ij}}{r_{ij}^6} \quad (1)$$

Received: September 17, 2014

Revised: November 25, 2014

Published: January 6, 2015



Table 1. Interionic Potential Pair Parameters Employed in the Present Study

X	$q_x$ (C)	$\sigma_x$ (Å)	$A_{\text{Na-X}}$ (eV)	$A_{\text{X-O}}$ (eV)	$C_{\text{X-O}}$ (eV·Å <sup>6</sup> )	$P_{\text{X-O}}$ (eV·Å <sup>4</sup> )
Na	0.65	1.13	2.298	0.1061	0.00	0.0
M = Ni	1.30	0.69	24.256	3.0846	59.85	31.0
M = Zn	1.30	0.74	21.965	3.4876	89.85	35.0
M = Co	1.30	0.79	16.431	2.8356	94.85	35.0
M = Mg	1.30	0.86	11.082	2.1508	115.85	35.0
Te	3.90	0.70	9.081	3.9098	17.15	11.3
O	−1.30	1.21	0.106	0.9260	85.14	0.0

$n_{ij}$  = 11, 9, or 7, respectively, for cation–cation, cation–anion, and anion–anion.

where  $q_i$  is the charge and  $\sigma_i$  is the ionic radius<sup>48</sup> of the  $i$ th ion. The parameters,  $A_{ij}$ ,  $P_{ij}$ , and  $C_{ij}$ , respectively, describe the overlap–repulsion energy of the electron clouds, the charge dipole interactions (in an average sense), and the dispersion constant, between ion pairs  $i$  and  $j$ . It has a softer overlap repulsion ( $1/r^n$ , where  $n$  = 11, 9, or 7, respectively, for cation–cation, cation–anion, and anion–anion pairs) compared to the more popular Born–Mayer (Buckingham) and Lennard–Jones potentials, more so between the anions. An optimized set of parameters for the entire family of  $\text{Na}_2\text{M}_2\text{TeO}_6$ , where  $M$  = Ni, Co, Zn, or Mg, is developed empirically (see Table 1) by fitting to their corresponding X-ray structure and conductivity at 600 K.<sup>34</sup> The fitting procedure followed here involves a series of MD simulations, each, typically, of 2 ns, with a refined set of parameters until various interatomic distances and local coordination numbers agree with the X-ray structure. After stabilizing the framework structure, the Na–Na and Na–O parameters are refined to reproduce the experimental conductivity.

**Simulation Details.** Employing the optimized set of parameters listed in Table 1 isothermal–isobaric ensemble molecular dynamics simulations (NPT–MD) are carried out at several temperatures, all at 1 atm pressure. The NPT–MD method, due to Parrinello–Rahman,<sup>49</sup> allows for changes in the shape as well as size of the simulation box. Simulations are started from their respective X-ray structures and with initial velocities sampled from a Gaussian distribution at the desired temperature. The rhombohedral unit cell is comprised of two formula units of  $\text{Na}_2\text{M}_2\text{TeO}_6$ . The simulation supercell in all cases included  $5 \times 5 \times 2$  unit cells comprising of 1100 ions ( $200\text{-Na}^+$ ,  $200\text{-M}^{2+}$ ,  $100\text{-Te}^{6+}$ , and  $600\text{-O}^{2-}$ ). A time step of 2 fs is used to evolve the trajectories. Typically the runs are 12 ns or longer, with trajectory samples stored at intervals of 200 fs for detailed analysis. However, a few long runs of 100 ns are carried to ensure convergence of properties, and also a few runs with larger systems consisting of  $6 \times 6 \times 3$  unit cells to ensure the adequacy of the system size. Periodic boundary conditions and the Ewald summation technique for the convergence of long-range Coulombic interactions are used. The NPT–MD simulations were performed with the software package LAMMPS.<sup>50</sup> Since the short-range part of the interaction potential (all except the Coulombic term in eq 1) is not available in the software, a tabulated form is used instead. A few micro canonical MD (NVE–MD) runs are also carried out (using our in-house software) for the Ni-containing system from which microscopic aspects such as the population and potential energy distribution of  $\text{Na}^+$  ions in a unit cell are calculated.

## RESULTS AND DISCUSSION

**Framework Structure.** The  $\text{Na}_2\text{M}_2\text{TeO}_6$  compounds, where  $M$  = Ni, Co, Zn, or Mg, has a layered structure of  $\text{TeO}_6$  and  $\text{MO}_6$  octahedra spanning the  $ab$ -plane of their hexagonal lattice (see Figure 1). The octahedral layers are held

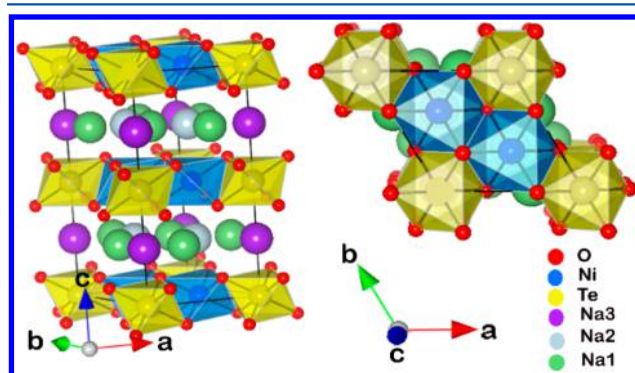


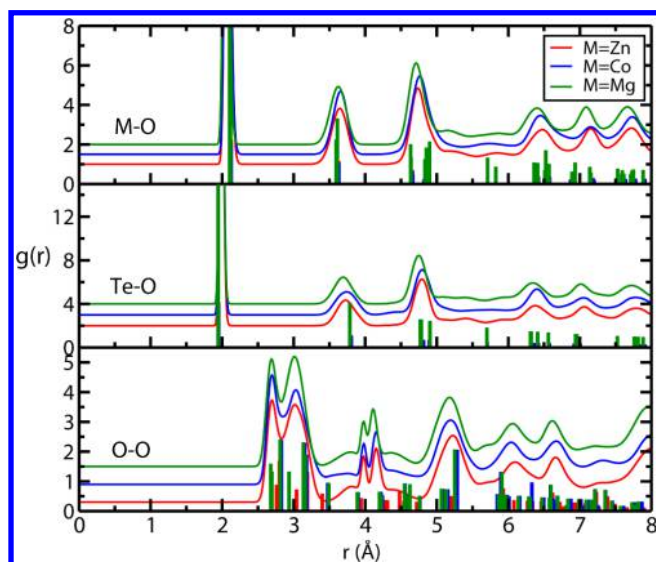
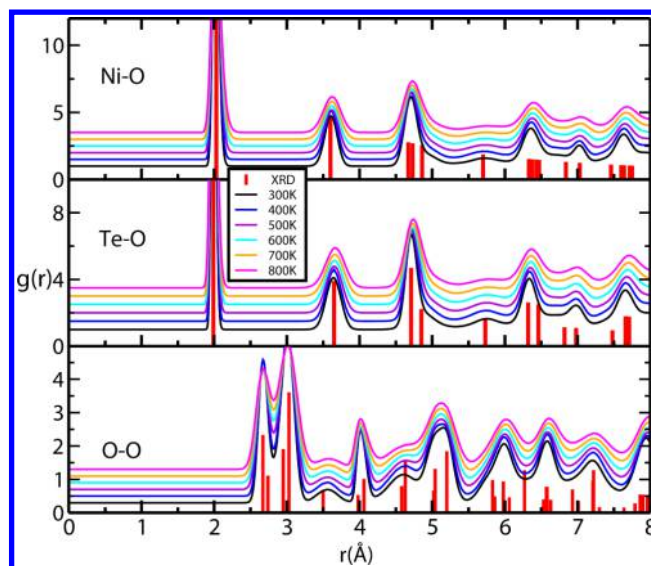
**Figure 1.** Views of the  $\text{Na}_2\text{Ni}_2\text{TeO}_6$  structure having edge-shared octahedral layers parallel to the  $ab$ -plane;  $\text{NiO}_6$ -octahedra (blue) and  $\text{TeO}_6$ -octahedra (yellow). One rhombohedral unit cell marked by black lines (left), along with the fringe atoms on the cell edges and oxygens (red) necessary for completing the octahedra are shown. The Na sites, Na1 (green), Na2 (light blue), and Na3 (violet), are also shown.

together along the  $c$ -axis by van der Waals forces and by interactions mediated through  $\text{Na}^+$  ions occupying their interlayers. The proposed interatomic potential retains these structural features in excellent agreement with the experiments. The average cell parameters of  $\text{Na}_2\text{M}_2\text{TeO}_6$  calculated from isothermal–isobaric ensemble molecular dynamics (NPT–MD) at 300 K is compared with room-temperature experimental values in Table 2. The calculated lattice parameters on substitution at the  $M$ -site follows the trend observed in experiments. The deviations from experimental values in all cases are well within one percent.

The radial distribution functions,  $g(r)$ , between select ion pairs,  $M$ –O,  $\text{Te}$ –O, and  $\text{O}$ –O, from NPT–MD simulations at 300 K for the  $\text{Na}_2\text{M}_2\text{TeO}_6$  compounds ( $M$  = Co, Zn, and Mg) are shown in Figure 2. The bar-plots are the corresponding  $g(r)$  based on room temperature X-ray structure.<sup>34</sup> All the peak locations in the simulated  $g(r)$  are consistent with their static  $g(r)$ , calculated for the X-ray structure, except for the thermal broadening. The Te and M ions make sharp six-coordinations with the oxygens in all cases, and the layer structure is retained intact. The average  $\text{Te}$ –O and  $M$ –O distances of the octahedra, for  $M$  = Ni, Zn, Co, and Mg, calculated from MD simulations (listed in Table 3), also show good agreement with the reported X-ray structure.<sup>34</sup>

**Table 2.** Average Lattice Parameters for  $\text{Na}_2\text{M}_2\text{TeO}_6$  from NPT-MD at 300 K are Compared with Experimental Results<sup>34</sup>

composition	space group	parameters	expt.	NPT-MD	$ \Delta $ (%)
$\text{Na}_2\text{Ni}_2\text{TeO}_6$	$P6_3/mcm$	$a$ (Å)	5.207	5.211	0.06
		$b$ (Å)	5.207	5.213	0.10
		$c$ (Å)	11.156	11.163	0.06
		$\alpha$	90.00	90.02	0.02
		$\beta$	90.00	89.97	0.03
		$\gamma$	120.00	120.04	0.03
$\text{Na}_2\text{Zn}_2\text{TeO}_6$	$P6_322$	$a$ (Å)	5.280	5.285	0.10
		$b$ (Å)	5.280	5.293	0.24
		$c$ (Å)	11.294	11.306	0.10
		$\alpha$	90.00	89.99	0.01
		$\beta$	90.00	89.95	0.05
		$\gamma$	120.00	120.16	0.13
$\text{Na}_2\text{Co}_2\text{TeO}_6$	$P6_322$	$a$ (Å)	5.289	5.283	0.12
		$b$ (Å)	5.289	5.269	0.38
		$c$ (Å)	11.214	11.202	0.11
		$\alpha$	90.00	89.51	0.54
		$\beta$	90.00	90.25	0.28
		$\gamma$	120.00	119.75	0.21
$\text{Na}_2\text{Mg}_2\text{TeO}_6$	$P6_322$	$a$ (Å)	5.254	5.240	0.10
		$b$ (Å)	5.254	5.246	0.24
		$c$ (Å)	11.255	11.225	0.26
		$\alpha$	90.00	90.21	0.23
		$\beta$	90.00	89.72	0.31
		$\gamma$	120.00	120.09	0.08

**Figure 2.** Radial distribution function (RDF),  $g(r)$ , between selected ion pairs, M–O ( $M = \text{Zn}, \text{Co}, \text{Mg}$ ), Te–O, O–O, of  $\text{Na}_2\text{M}_2\text{TeO}_6$  at room temperature. The  $g(r)$ s calculated for the X-ray structure are shown as vertical bars with intensity scaled down for clarity. The functions are displaced uniformly along Y-axis for clarity.**Figure 3.** Radial distribution function,  $g(r)$ , between selected ion pairs, Ni–O, Te–O, O–O, for  $\text{Na}_2\text{Ni}_2\text{TeO}_6$  over 300–800 K. The vertical bars in red are the corresponding  $g(r)$ s based on X-ray structure (intensity scaled down for clarity).<sup>34</sup> The functions are displaced uniformly along the Y-axis for clarity.

For the Ni-containing system the Te–O, Ni–O, and O–O  $g(r)$ s are calculated over the range of 300–800 K (Figure 3) to demonstrate the stability of the system. Slight reduction in the intensities accompanied by thermal broadening of the peaks is observed with temperature. However, the first peaks for the octahedral species remain well resolved, throughout the range, reflecting their sharp coordination with oxygens. These results demonstrate that proposed interatomic potential support the experimental structure of  $\text{Na}_2\text{M}_2\text{TeO}_6$ , where  $M = \text{Ni}, \text{Co}, \text{Zn}$ , and  $\text{Mg}$ , over a wide range of temperatures.

**Ionic Conductivity.** The  $\text{Na}^+$  ions occupy the interlayers of the polyhedral sheets, and are loosely bound to the framework facilitating ionic conductivity. Evidently the closely packed octahedral layers restrict the  $\text{Na}^+$  motion along the  $c$ -axis of the cell resulting in two-dimensional conductivity. The mean squared displacements (MSD) of the  $\text{Na}^+$  is calculated as a function of time are highly anisotropic when resolved along the cell edges. The MSD of  $\text{Na}^+$  along the  $c$ -axis converges rapidly, suggesting a value of about 0.2 Å for their thermal amplitudes. The MSD of  $\text{Na}^+$  parallel to the conducting layer at 600 K is shown in Figure 4 for all compositions. The MSDs for the  $\text{Na}_2\text{M}_2\text{TeO}_6$  show a systematic decrease across the series, Ni, Zn, Co, and Mg, in qualitative agreement with their measured conductivities. The framework ions,  $M = \text{Ni}, \text{Zn}, \text{Co}$  or  $\text{Mg}$ , Te, and O, do not diffuse over the temperature range examined here. The MSDs of the framework species for the Ni-system at 600 K is shown in the inset of Figure 4.

Following Einstein's relation, the self-diffusion coefficient of  $\text{Na}^+$  is calculated for the two-dimensional transport as

**Table 3.** Average Interatomic Distances (in Å) for the Te–O and M–O Octahedra ( $M = \text{Ni}, \text{Zn}, \text{Co}$ , and  $\text{Mg}$ ) from NPT-MD Simulations at 300 K

M	Ni		Zn		Co		Mg	
	expt.	MD	expt.	MD	expt.	MD	expt.	MD
Te–O	1.993	1.990	1.971	1.990	1.951	1.990	1.945	1.990
M–O	2.035	2.020	2.148	2.070	2.112	2.070	2.105	2.050



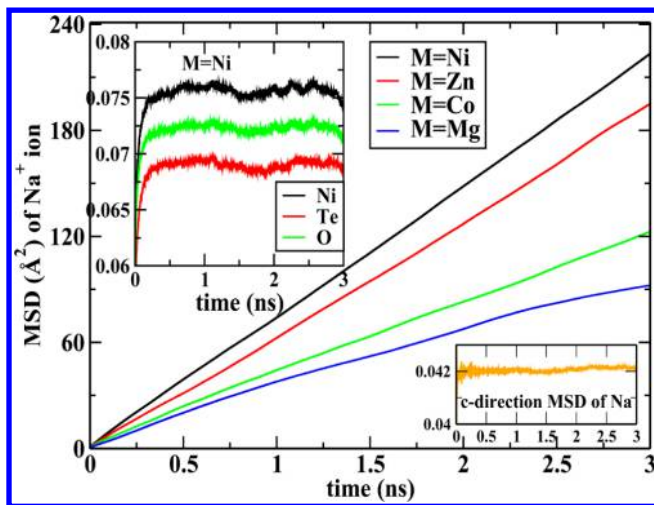


**Figure 4.** Mean square displacement (MSD) of  $\text{Na}^+$  ions in  $\text{Na}_2\text{M}_2\text{TeO}_6$  from MD simulation at 600 K. MSD of  $\text{Na}^+$  along the  $c$ -direction shown in the inset (bottom-right) demonstrates the anisotropic nature of the  $\text{Na}^+$  transport in the system. The MSDs of the framework species for  $\text{Na}_2\text{Ni}_2\text{TeO}_6$  at 600 K is shown in the inset (top-left).

$$D = \lim_{t \rightarrow \infty} \frac{1}{4Nt} \left\langle \sum_{j=1}^N [\vec{r}_j(t) - \vec{r}_j(0)]^2 \right\rangle \quad (2)$$

where  $N$  is the number of  $\text{Na}^+$  in the system,  $\vec{r}_j(t)$  is the position vector of the  $j$ th ion at time  $t$ , and the angular bracket indicates the average over several time origins. The ionic conductivity of the system is calculated from the Nernst–Einstein relation

$$\sigma = \frac{nq^2D}{k_B T} \quad (3)$$

where  $n$  is the number density of  $\text{Na}^+$  in the system,  $q$  is the formal charge of  $\text{Na}^+$  (that is,  $+1e$ ),  $k_B$  is the Boltzmann constant, and  $T$  is the temperature in Kelvin. For the Ni-system the conductivity is calculated over 500–800 K from NPT-MD simulations employing eqs 2 and 3. The Arrhenius plots,  $\log(\sigma T)$  versus inverse of temperature, presented in Figure 5 shows deviation from linearity, suggesting non-Arrhenius behavior. Overall, the simulation results are in very good agreement with previous experimental observations.

**Microscopics of  $\text{Na}^+$  Transport.** The X-ray studies have proposed three  $\text{Na}^+$  sites at the interlayer of  $\text{Na}_2\text{M}_2\text{TeO}_6$ . Labeled Na1, Na2, and Na3, these sites have a multiplicity of 3, 2, and 1, respectively, per interlayer per unit cell. All these sites have a trigonal-prismatic arrangement of oxygen ions. The octahedral layers include tetrahedral holes formed between two neighboring  $\text{NiO}_6$  and a  $\text{TeO}_6$  octahedron (see Figure 1). Na1 site is located midway between the two tetrahedral holes from the top and bottom layers. Na2 sites are sandwiched between the triangular faces of  $\text{NiO}_6$  octahedra from the top and bottom layers, while Na3 between two  $\text{TeO}_6$  octahedra. The calculated Na–O radial distribution functions,  $g(r)$ , presented in Figure 6, have broad features owing to the  $\text{Na}^+$  diffusion but shows an average coordination of about 6 over  $3.2 \text{ \AA}$  (up to the minimum following its first peak). The  $g(r)$  of the Na-sites with oxygens (based on the X-ray structure) is shown as a bar-plot. The first peak positions of the simulated Na–O  $g(r)$  are off by  $0.2 \text{ \AA}$  with

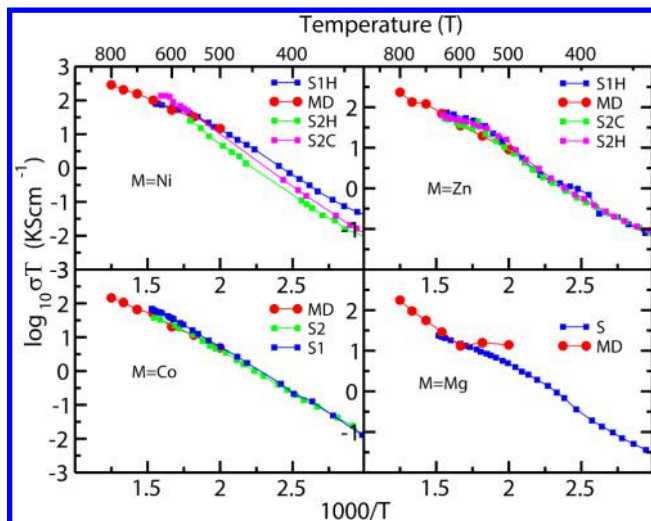


**Figure 5.** Arrhenius plot of  $\text{Na}^+$  conductivity for  $\text{Na}_2\text{M}_2\text{TeO}_6$ , where  $M = \text{Ni, Co, Zn, or Mg}$ , from MD simulation (shown as red dots) over 500–800 K. The experimental data shown are extracted from a high resolution copy of Figure 8 of Evstigneeva et al.<sup>34</sup> S1 and S2 are sample numbers; H and C abbreviate heating and cooling cycles, as reported in their original experimental report.

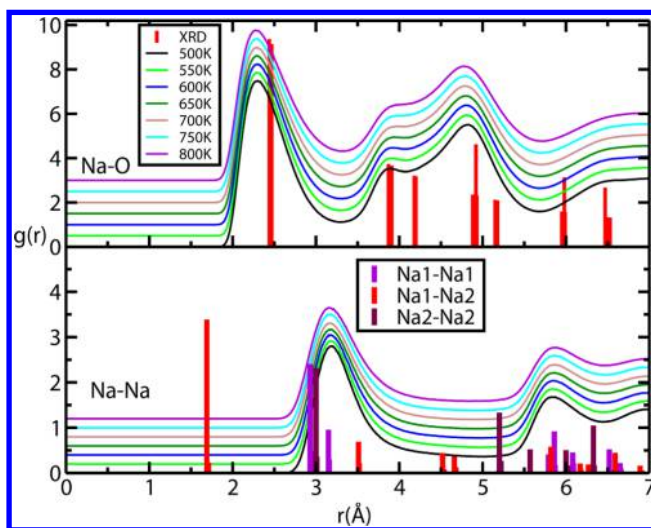


**Figure 6.** Radial distribution functions,  $g(r)$ , for pairs Na–O (top) and Na–Na (bottom) in  $\text{Na}_2\text{Ni}_2\text{TeO}_6$ . The distribution of Na-sites, Na1–Na1, Na1–Na2, and Na2–Na2, for the X-ray structure is shown as vertical bars. A few select site–site distances are Na1–Na1 =  $2.93 \text{ \AA}$  (1st neighbor),  $3.15 \text{ \AA}$  (2nd), Na2–Na2 =  $3.00 \text{ \AA}$ , and Na1–Na2 =  $1.69 \text{ \AA}$  (1st),  $3.51 \text{ \AA}$  (2nd). The functions are displaced uniformly along  $Y$ -axis for clarity.

respect to the X-ray structure, suggesting that the  $\text{Na}^+$  ions populate these sites slightly off-centered.

Employing a spherical cutoff of  $0.8 \text{ \AA}$ , the  $\text{Na}^+$  counts at the various sites have been estimated from the MD trajectory at 600 K. The estimated populations at Na1 and Na2 sites are roughly 50%, with Na3 measuring practically none. The population estimated are in qualitative agreement with Evstigneeva et al.<sup>34</sup> The Na–Na  $g(r)$ s in Figure 6 present a liquid-like distribution of the  $\text{Na}^+$  ions. Prominent in the  $g(r)$  is the absence of intensity around  $1.7 \text{ \AA}$  corresponding to the nearest Na1–Na2 separation, which suggest that, while an Na1 site is occupied by an  $\text{Na}^+$ , its nearest Na2 locations are vacant, and vice versa. However, simultaneous occupancy of two

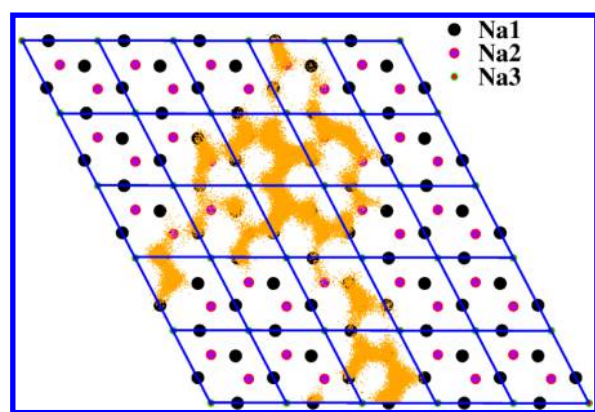


**Figure 7.** MD trajectories of a randomly picked  $\text{Na}^+$  ion during 5.4 ns at 600 K is shown superimposed over the Na-site distribution.

neighboring Na1 sites (at distances 2.93 and 3.15 Å) and two neighboring Na2 sites (at 3.00 Å) are permitted. The absence of a peak around 4.5–4.7 Å, which corresponds to the third and fourth Na2 neighbors of a Na1 site, also suggests the strong ion–ion correlation. Similar deduction may be attributed to the low intensity around 5.2 Å corresponding to the separation between two next-neighboring Na2 sites. This intermediate-range correlation of the Na-sublattice is evidently mediated through the  $\text{Na}^+$  ions itself.

The trajectory of a single, randomly picked,  $\text{Na}^+$  is displayed superimposed over the various Na sites of the simulation cell for an exposure time of 5.4 ns (see Figure 7). The  $\text{Na}^+$  is seen to develop a well-connected pathway spread across several unit cells over this period. While the Na1 and Na2 sites form the nodal-points of its trajectory, the Na3 sites are hardly visited.

The potential energy of individual  $\text{Na}^+$  ions is calculated as

$$V_i = \frac{1}{2} \sum_{\substack{j=1 \\ j \neq i}}^{N_t} V_{ij} \quad (4)$$

where  $N_t$  is the total number of particles in the system and  $V_{ij}$  is the interaction potential in eq 1, such that the total potential energy of the system is

$$V_t = \sum_{i=1}^{N_t} V_i \quad (5)$$

The potential energy of  $\text{Na}^+$  ions is calculated as in eq 4, sampled on a fine two-dimensional grid on the ab-plane spanning one unit cell (with all  $\text{Na}^+$  coordinates also folded in to a single cell) and averaged over 60000 configurations over a 12 ns long NVE-MD simulation at 600 K. Figure 8 (left) displays the potential energy surface (PES) of  $\text{Na}^+$  ions thus generated (replicated over  $2 \times 2$  unit cells for ease of visualization of its continuity). The Na2 site presents the deepest of minima of about  $-2.65$  eV and with a basin of about 1 Å radius, while a very shallow minimum of  $-2.45$  eV is observed at Na1. The energies at Na3 are much higher, above  $-2.32$  eV, and do not play any active role in  $\text{Na}^+$  transport. The deeper minima at Na2, being located between two  $\text{NiO}_6$  octahedra, can be attributed to the relatively low repulsion  $\text{Na}^+$  with  $\text{Ni}^{2+}$ .

Interestingly, the population profile of  $\text{Na}^+$  shown in Figure 8 (right) presents a contrasting picture to the potential energy profile shown on the left. Na1 sites show high population of  $\text{Na}^+$  though these sites do not correspond to a minimum in the potential energy profile in Figure 8 (left). We shall note that the population in terms of a reaction coordinate,  $\lambda$ , is proportional to the Boltzmann probability,<sup>51</sup>

$$P(\lambda) = \frac{e^{-F(\lambda)/kT}}{Z} \quad (6)$$

where  $Z$  is the classical partition function at temperature  $T$ , and  $k$  is the Boltzmann constant. The free-energy,  $F(\lambda) = U(\lambda) - TS(\lambda)$ , where  $U(\lambda)$  and  $S(\lambda)$  are, respectively, the internal energy and entropy at temperature  $T$ . The reaction coordinate,  $\lambda$ , in the present case may be identified with spacial coordinates on the  $a$ – $b$  plane, and in the “mean-field” sense, the potential energy landscape in Figure 8 (left-panel) represents the  $U(\lambda)$  above. Thus, the free-energy profile of the  $\text{Na}^+$  ions can be obtained by “inverting” the population profile shown in Figure 8 (right-panel). A minima of the potential energy,  $U(\lambda)$ , or a gain in entropy,  $S(\lambda)$ , brings about population at the sites. Now the absence of an appreciable minima in  $U(\lambda)$  around the Na1

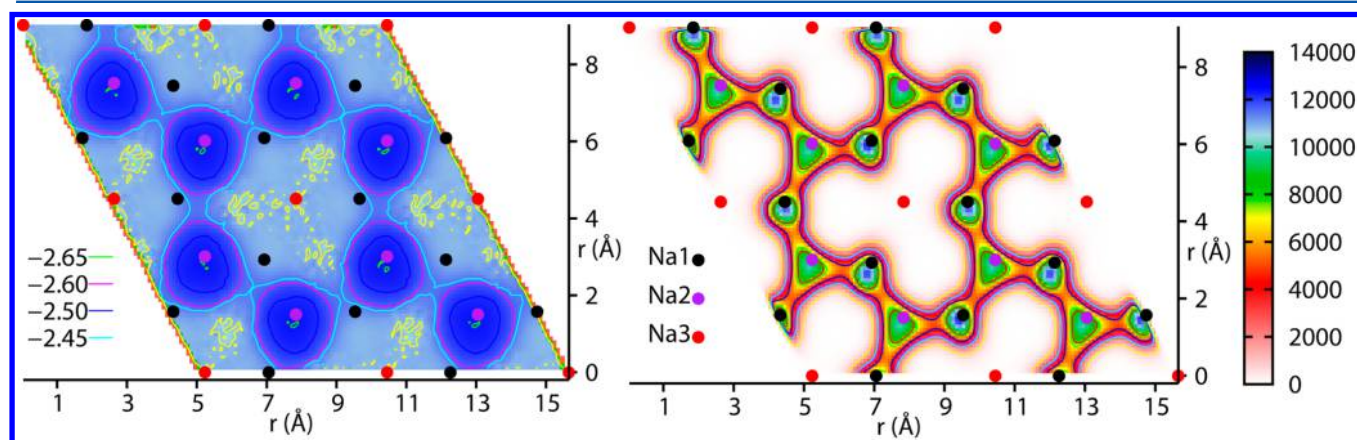


**Figure 8.** (Left-panel) The average individual potential energy (as in eq 4), and (right-panel) population profile (un-normalized) of  $\text{Na}^+$  ions from MD simulations at 600 K (mapped on to  $2 \times 2$  unit cells). The locations of the Na sites, Na1, Na2, and Na3, from an X-ray study<sup>34</sup> are marked by the common legends shown in the middle. The population contours reflects that the preferred migration pathway of  $\text{Na}^+$  is Na1–Na2–Na1. The qualitative difference between the two distributions are attributed to the ion–ion correlations and entropic contributions (see text for detailed discussion).



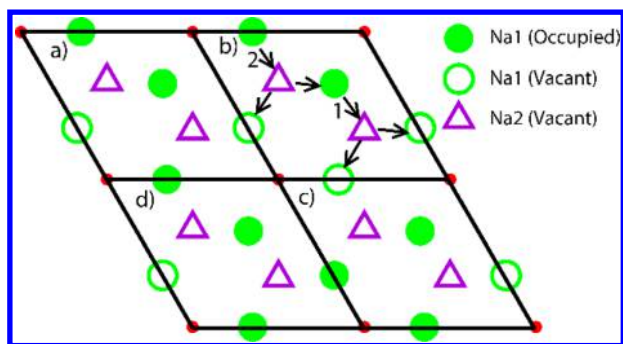


**Figure 9.** Schematic diagram of  $\text{Na}^+$ -hopping mechanism in  $\text{Na}_2\text{Ni}_2\text{TeO}_6$ . The Na1 and Na2 sites in over  $2 \times 2$  unit cells, marked a–d, per interlayer are shown. The open and filled symbols represent, respectively, the vacant and occupied sites. Refer to text for details.

site in Figure 8 (left-panel), despite their significant population, suggests entropic contributions.

A well-developed migration pathway of  $\text{Na}^+$  connecting Na1–Na2–Na1 emerges from the population profile in Figure 8 (right). Insight into the mechanism of  $\text{Na}^+$  transport through Na1–Na2–Na1 sites can be understood, invoking the role of ion–ion correlations, in the backdrop of the topology of Na site’s network. We shall note that there are three Na1 and two Na2 sites available for the two  $\text{Na}^+$  ions per interlayer per unit cell of the system. Each Na1 has two neighboring Na2 sites at a distance of about 1.7 Å, and each Na2 has three Na1 neighbors at this distance. We shall, further, note that the ion–ion repulsion prohibits two  $\text{Na}^+$  comes closer than 2.5 Å, as is evidenced in the Na–Na  $g(r)$  shown in Figure 6. We shall consider a few representative scenarios to arrange two  $\text{Na}^+$  ions over the five Na sites (three Na1 and two Na2) available per interlayer per unit cell:

- (1) Two  $\text{Na}^+$  occupy the two energetically favorable Na2 sites is “too perfect” an arrangement, leaving no room for  $\text{Na}^+$  transport in the system, since a  $\text{Na}^+$  hop to any one of the three vacant Na1 neighbors brings it closer to another  $\text{Na}^+$  by 1.7 Å (occupying the other Na1 site). In other words, this arrangement restricts the accessible configurations and thus entropically unfavorable.
- (2)  $\text{Na}^+$  ions occupy a Na1 site inside the unit cell along with two other Na1 sites on opposite cell edges, such that the total of two  $\text{Na}^+$  per interlayer per unit cell is accounted for. This amount to one Na1 site per cell (to be precise, two Na1’s on two opposite cell edges contributing half) free for occupancy. The cell marked (a) in Figure 9 provides a schematic representation of this situation. However, this leaves the vacant Na1 site inaccessible as the Na2 site on its path remains unfavorable for the necessary “stop-over” of an  $\text{Na}^+$  due to its shorter distance to one of the occupied Na1 sites.
- (3) Na1 sites at all four cell edges occupied, leaving the one inside the cell vacant, also leads to a similar “road-block”, as in scenario 2.
- (4) Having exhausted the ordered arrangements, another scenario incorporating some degree of disorder into the  $\text{Na}^+$  sublattice shall be examined. In Figure 9, for instance, the unit cell marked *a* has arrangements, as in scenario 2 above, and accounts for 2  $\text{Na}^+$  per cell. Starting from scenario 2 a disorder is created, where a  $\text{Na}^+$  at the edge, shared by cells *b* and *c*, is moved to the edge shared by cells *c* and *d*. Now cell *b* accounts for only

one and half  $\text{Na}^+$ , while cell *d* includes two and half. This arrangement, however, allows for  $\text{Na}^+$  hops from Na1 to Na2 sites in cell *b*, as shown by arrow numbered 1, and further bifurcations to neighboring Na1 sites. The event can be followed by  $\text{Na}^+$  hops shown by arrow labeled 2. This process can propagate across the lattice and the system gains in terms of entropy, as more sites are now accessible to the  $\text{Na}^+$  ions.

We shall, however, note that scenario 4 above is just one of several proposals where disorder of the Na-sublattice increases the entropy (and, consequently, decreases the free energy as), facilitating  $\text{Na}^+$  transport in the system. This explains the significant  $\text{Na}^+$  population at Na1 site despite their relatively higher energy. The topology of the network of Na sites demand that some degree of  $\text{Na}^+$  disorder is essential for fast ion transport in  $\text{Na}_2\text{M}_2\text{TeO}_6$ . Further, the situation also proposes that the high degree of ion–ion correlation prevailing necessitates a cooperative mechanism to be operative in this system.

## CONCLUSION

An interatomic potential is proposed for  $\text{Na}_2\text{M}_2\text{TeO}_6$ , a family of fast ion solids, where M = Ni, Co, Zn, or Mg. The potential model reproduces the structure, conductivity, and population of  $\text{Na}^+$  at different Na sites, in excellent quantitative agreement with experiments. Fresh insight on the microscopic aspects of ion transport is provided. The results suggest that ion–ion correlation and disordered  $\text{Na}^+$  sublattice are key features to fast ion transport in these systems.

Available experimental results hint upon the remarkable robustness of the generic framework of  $\text{Na}_2\text{M}_2\text{TeO}_6$  solids in admitting such diverse ion substitutions, such as, for example, Li and Fe at the M-site, resulting in stable  $\text{Na}_2\text{LiFeTeO}_6$ , which is interestingly a  $\text{Na}^+$  conductor.<sup>41</sup> It is hoped that the present work would stimulate more computational studies on this promising class of solids; investigation of the substitutional effect on fast ion transport in the system, for instance, would be particularly interesting.

## AUTHOR INFORMATION

### Corresponding Author

\*E-mail: padmakumarp@iitg.ernet.in. Phone: +91-3612582718.

### Notes

The authors declare no competing financial interest.

## ACKNOWLEDGMENTS

The authors acknowledge financial support (Grant No: SR/S1/PC-24/2011) from Department of Science and Technology, New Delhi. We are grateful to Dr. M. A. Evstigneeva for providing us with high resolution images of their conductivity plots. One of the authors (K.S.) acknowledges Dr. S. Roy for useful discussions.

## REFERENCES

- (1) Kendrick, E.; Slater, P. Battery and solid oxide fuel cell materials. *Annu. Rep. Prog. Chem., Sect. A* **2012**, *108*, 424–448.
- (2) Tiwari, J. N.; Tiwari, R. N.; Kim, K. S. Zero-dimensional, one-dimensional, two-dimensional and three-dimensional nanostructured materials for advanced electrochemical energy devices. *Prog. Mater. Sci.* **2012**, *57*, 724–803.
- (3) Catlow, C.; Guo, Z.; Miskufova, M.; Shevlin, S.; Smith, A.; Sokol, A.; Walsh, A.; Wilson, D.; Woodley, S. Advances in computational

studies of energy materials. *Philos. Trans. R. Soc. A* **2010**, 368, 3379–3456.

(4) Kawamura, J.; Asayama, R.; Kuwata, N.; Kamishima, O. Ionic transport in glass and polymer: Hierarchical structure and dynamics. *Phys. Solid State Ionics* **2006**, 193–246.

(5) Kulkarni, A.; Maiti, H.; Paul, A. Fast ion conducting lithium glasses: review. *Bull. Mater. Sci.* **1984**, 6, 201–221.

(6) Swenson, J.; Börjesson, L. Correlation between free volume and ionic conductivity in fast ion conducting glasses. *Phys. Rev. Lett.* **1996**, 77, 3569.

(7) Hayashi, A.; Noi, K.; Sakuda, A.; Tatsumisago, M. Superionic glass-ceramic electrolytes for room-temperature rechargeable sodium batteries. *Nat. Commun.* **2012**, 3, 856.

(8) Bron, P.; Johansson, S.; Zick, K.; Schmedt auf der Gönne, J. r.; Dehnen, S.; Roling, B.  $\text{Li}_{10}\text{SnP}_2\text{S}_{12}$ : An affordable lithium superionic conductor. *J. Am. Chem. Soc.* **2013**, 135, 15694–15697.

(9) Masquelier, C. Solid electrolytes: Lithium ions on the fast track. *Nat. Mater.* **2011**, 10, 649–650.

(10) Kamaya, N.; Homma, K.; Yamakawa, Y.; Hirayama, M.; Kanno, R.; Yonemura, M.; Kamiyama, T.; Kato, Y.; Hama, S.; Kawamoto, K. A lithium superionic conductor. *Nat. Mater.* **2011**, 10, 682–686.

(11) Adams, S.; Rao, R. P. Structural requirements for fast lithium ion migration in  $\text{Li}_{10}\text{GeP}_2\text{S}_{12}$ . *J. Mater. Chem.* **2012**, 22, 7687–7691.

(12) Takada, K. Progress and prospective of solid-state lithium batteries. *Acta Mater.* **2013**, 61, 759–770.

(13) Sahu, G.; Lin, Z.; Li, J.; Liu, Z.; Dudney, N.; Liang, C. Air-stable, high-conduction solid electrolytes of arsenic-substituted  $\text{Li}_4\text{SnS}_4$ . *Energy Environ. Sci.* **2014**, 7, 1053–1058.

(14) Thangadurai, V.; Narayanan, S.; Pinzaru, D. Garnet-type solid-state fast Li ion conductors for Li batteries: critical review. *Chem. Soc. Rev.* **2014**, 43, 4714–4727.

(15) Park, M.; Zhang, X.; Chung, M.; Less, G. B.; Sastry, A. M. A review of conduction phenomena in Li-ion batteries. *J. Power Sources* **2010**, 195, 7904–7929.

(16) Sathiy, M.; Ramesha, K.; Rousse, G.; Foix, D.; Gonbeau, D.; Guruprakash, K.; Prakash, A.; Doublet, M.; Tarascon, J.-M.  $\text{Li}_4\text{NiTeO}_6$  as a positive electrode for Li-ion batteries. *Chem. Commun.* **2013**, 49, 11376–11378.

(17) Saranya, K.; Deviannapoorani, C.; Dhivya, L.; Ramakumar, S.; Janani, N.; Murugan, R.  $\text{Li}_{7-x}\text{La}_3\text{Sn}_{2-x}\text{Nb}_x\text{O}_{12}$  ( $x = 0.25-1$ ) cubic lithium garnet. *Mater. Lett.* **2012**, 77, 57–59.

(18) Etacheri, V.; Marom, R.; Elazari, R.; Salitra, G.; Aurbach, D. Challenges in the development of advanced Li-ion batteries: a review. *Energy Environ. Sci.* **2011**, 4, 3243–3262.

(19) Hueso, K. B.; Armand, M.; Rojo, T. High temperature sodium batteries: status, challenges and future trends. *Energy Environ. Sci.* **2013**, 6, 734–749.

(20) Aniya, M. Understanding the mechanism of superionic transport from trends of materials properties. *Phys. Procedia* **2013**, 44, 25–34.

(21) Mehrer, H. *Diffusion in solids: fundamentals, methods, materials, diffusion-controlled processes*; Springer: New York, 2007; Vol. 155.

(22) Hull, S. Superionics: crystal structures and conduction processes. *Rep. Prog. Phys.* **2004**, 67, 1233.

(23) Islam, M. S.; Fisher, C. A. Lithium and sodium battery cathode materials: computational insights into voltage, diffusion and nano-structural properties. *Chem. Soc. Rev.* **2014**, 43, 185–204.

(24) Vashishta, P.; Rahman, A. Ionic motion in  $\alpha\text{-AgI}$ . *Phys. Rev. Lett.* **1978**, 40, 1337.

(25) Vashishta, P.; Kalia, R. K.; Rino, J. P.; Ebbsjö, I. Interaction potential for  $\text{SiO}_2$ : a molecular-dynamics study of structural correlations. *Phys. Rev. B* **1990**, 41, 12197.

(26) Walker, J.; Catlow, C. Structure and transport in non-stoichiometric  $\beta\text{-Al}_2\text{O}_3$ . *J. Phys. C: Solid State Phys.* **1982**, 15, 6151.

(27) Malavasi, L.; Fisher, C. A.; Islam, M. S. Oxide-ion and proton conducting electrolyte materials for clean energy applications: structural and mechanistic features. *Chem. Soc. Rev.* **2010**, 39, 4370–4387.

(28) Kendrick, E.; Kendrick, J.; Knight, K. S.; Islam, M. S.; Slater, P. R. Cooperative mechanisms of fast-ion conduction in gallium-based oxides with tetrahedral moieties. *Nat. Mater.* **2007**, 6, 871–875.

(29) Roy, S.; Kumar, P. P. Influence of Si/P ordering on  $\text{Na}^+$  transport in NASICONs. *Phys. Chem. Chem. Phys.* **2013**, 15, 4965–4969.

(30) Roy, S.; Kumar, P. P. Influence of Cationic ordering on ion transport in NASICONs: Molecular dynamics study. *Solid State Ionics* **2013**, 253, 217–222.

(31) Taskin, A.; Lavrov, A.; Ando, Y. Achieving fast oxygen diffusion in perovskites by cation ordering. *Appl. Phys. Lett.* **2005**, 86, 091910–091910–3.

(32) Taskin, A.; Lavrov, A.; Ando, Y. Fast oxygen diffusion in A-site ordered perovskites. *Prog. Solid State Chem.* **2007**, 35, 481–490.

(33) Parfitt, D.; Chroneos, A.; Tarancón, A.; Kilner, J. A. Oxygen ion diffusion in cation ordered/disordered  $\text{GdBaCo}_2\text{O}_{5+\delta}$ . *J. Mater. Chem.* **2011**, 21, 2183–2186.

(34) Evstigneeva, M. A.; Nalbandyan, V. B.; Petrenko, A. A.; Medvedev, B. S.; Kataev, A. A. A new family of fast sodium ion conductors:  $\text{Na}_2\text{M}_2\text{TeO}_6$  ( $\text{M} = \text{Ni}, \text{Co}, \text{Zn}, \text{Mg}$ ). *Chem. Mater.* **2011**, 23, 1174–1181.

(35) Gupta, A.; Buddie Mullins, C.; Goodenough, J. B.  $\text{Na}_2\text{Ni}_2\text{TeO}_6$ : Evaluation as a cathode for sodium battery. *J. Power Sources* **2013**, 243, 817–821.

(36) Kumar, V.; Gupta, A.; Uma, S. Formation of honeycomb ordered monoclinic  $\text{Li}_2\text{M}_2\text{TeO}_6$  ( $\text{M} = \text{Cu}, \text{Ni}$ ) and disordered orthorhombic  $\text{Li}_2\text{Ni}_2\text{TeO}_6$  oxides. *Dalton Trans.* **2013**, 42, 14992–14998.

(37) Hafskjold, B.; Li, X. Molecular dynamics simulations of the  $\text{Mg}^{2+}$ -stabilized  $\text{Na}^+$ -beta-alumina. *J. Phys.: Condens. Matter* **1995**, 7, 2949.

(38) Zendejas, M. A.; Thomas, J. O. Conduction mechanisms in Solid electrolytes:  $\text{Na}^+$  beta-alumina. *Phys. Scr.* **1990**, 1990, 235.

(39) Edvardsson, S.; Ojamae, L.; Thomas, J. O. A study of vibrational modes in  $\text{Na}^+$  beta-alumina by molecular dynamics simulation. *J. Phys.: Condens. Matter* **1994**, 6, 1319.

(40) Skotniczny, Z.; MoScinski, J.; Rycerz, Z. Computer simulation studies of cation migration mechanisms in sodium beta-alumina. *J. Phys. C: Solid State Phys.* **1986**, 19, 4781.

(41) Nalbandyan, V.; Petrenko, A.; Evstigneeva, M. Heterovalent substitutions in  $\text{Na}_2\text{M}_2\text{TeO}_6$  family: Crystal structure, fast sodium ion conduction and phase transition of  $\text{Na}_2\text{LiFeTeO}_6$ . *Solid State Ionics* **2013**, 233, 7–11.

(42) Parrinello, M.; Rahman, A.; Vashishta, P. Structural transitions in superionic conductors. *Phys. Rev. Lett.* **1983**, 50, 1073.

(43) Nomura, K.-i.; Yokoyama, Y.; Kobayashi, M. Particle correlation in  $\alpha\text{-AgI}$ . *Solid State Ionics* **2002**, 154, 285–289.

(44) Boolchand, P.; Bresser, W. Mobile silver ions and glass formation in solid electrolytes. *Nature* **2001**, 410, 1070–1073.

(45) Ivanov-Schitz, A.; Savvin, S.; Mazo, G. Cationic transport mechanism in  $\alpha\text{-Ag}_{1-x}\text{Cu}_x\text{I}$  ( $0 < x < 0.25$ ): Molecular-dynamics simulation. *Crystallogr. Rep.* **2009**, 54, 292–298.

(46) Kumar, P. P.; Yashonath, S. A full interionic potential for  $\text{Na}_{1+x}\text{Zr}_2\text{Si}_{3-x}\text{O}_{12}$  superionic conductors. *J. Am. Chem. Soc.* **2002**, 124, 3828–3829.

(47) Roy, S.; Kumar, P. P. Framework flexibility of sodium zirconium phosphate: role of disorder, and polyhedral distortions from Monte Carlo investigation. *J. Mater. Sci.* **2012**, 47, 4946–4954.

(48) Huheey, J. E.; Keiter, E. A.; Keiter, R. L.; Medhi, O. K. *Inorganic Chemistry: Principles of Structure and Reactivity*; Pearson Education: India, 2006.

(49) Parrinello, M.; Rahman, A. Polymorphic transitions in single crystals: A new molecular dynamics method. *J. Appl. Phys.* **1981**, 52, 7182–7190.

(50) Parks, M. L.; Plimpton, S. J.; Lehoucq, R. B.; Silling, S. A. Peridynamics with LAMMPS: A user guide. *Sandia National Laboratory Report, SAND2008–0135*; Sandia National Laboratory: Albuquerque, New Mexico, 2008.



(51) Reif, F. *Fundamentals of Statistical and Thermal Physics*; McGraw-Hill: Columbus, OH, 1985.